Climate Dynamics
https://doi.org/10.1007/s00382-024-07434-5

ORIGINAL ARTICLE

Chile Niño/Niña in the coupled model intercomparison project phases 5 and 6

Emilio Concha[1] · Boris Dewitte[1,2,3] · Cristian Martinez-Villalobos[4,5] · Fabien Solmon[6] · Emilia Sanchez-Gomez[1]

Received: 12 April 2024 / Accepted: 30 August 2024

Abstract
The north and central coast of Chile is influenced by El Niño-Southern Oscillation (ENSO) through oceanic and atmospheric teleconnections. However, it also experiences episodic oceanic warmings off central Chile (30°S) lasting a few months that are not necessarily associated with ENSO. These episodes, called "Chile Niño" events, besides their ecological and socio-economical impacts, have also the potential to influence tropical Pacific variability. Here, we investigate how realistically the models in the Coupled Model Intercomparison Project (CMIP, Phases 5 and 6) simulate Chile Niño/Niña (CN) events, and quantify their changes under anthropogenic forcing. Despite limitations of the global models in simulating realistically coastal upwelling dynamics, we show that they simulate reasonably well the observed spatial pattern, amplitude and seasonal evolution of CN events. They however fail to properly represent the positive skewness from observations. The analysis of a sub-group of models (36) that simulate ENSO realistically reveals that CN events increase in amplitude and variance in the future climate with no changes in their frequency of occurence. This is interpreted as resulting from compensating effects amongst changes in remote drivers and local feedbacks. In particular, ENSO variance increases while that of the South Pacific Oscillation decreases. Conversely, we found that while the Wind-Evaporation-SST feedback tends to increase and the coupling between mixed-layer depth and SST weakens, favoring the development of CN events, the thermocline and wind-SST feedbacks decrease. However, only the change in the thermocline feedback is correlated to changes in CN variance amongst the models, suggesting a dominant role of local oceanic stratification changes in constraining the sensitivity of CN to global warming.

Keywords Coastal Niño/Niña · South eastern Pacific · Air–sea interactions · Climate change · CMIP models

1 Introduction

Basin-scale climate modes in the tropics are important drivers of both the ocean and atmospheric circulation near continent boundaries, which impacts socio-ecological systems in the densely populated coastal regions. In the Pacific, the El Niño-Southern Oscillation (ENSO) phenomenon, the most emblematic interannual mode of variability at the global scale, has for instance far reaching consequences on society all around the Pacific (McPhaden et al. 2006; Holbrook et al. 2020a), with damaging impact over the global economy (Liu et al. 2023). Eastern boundary upwelling systems (EBUS) are particularly sensitive to basin-scale tropical modes due to the efficient equatorial oceanic teleconnection that propagates thermocline fluctuations along the coast at high-latitudes (Sprintall et al. 2020). In addition, in these systems the process of upwelling maintains a shallow mixed-layer and an on-shoreward sloping thermocline, which favors local air-sea

✉ Emilio Concha
concha@cerfacs.fr

[1] CECI, Université de Toulouse III, CERFACS/CNRS, Toulouse, France

[2] Centro de Estudios Avanzados en Zonas Áridas (CEAZA), Coquimbo, Chile

[3] Center for Ecology and Sustainable Management of Oceanic Islands (ESMOI), Departamento de Biología Marina, Facultad de Ciencias del Mar, Universidad Católica del Norte, Coquimbo, Chile

[4] Faculty of Engineering and Science, Universidad Adolfo Ibáñez, Santiago, Chile

[5] Data Observatory Foundation, ANID Technology, Center No. DO210001, Santiago, Chile

[6] Laboratoire d'Aérologie, Université de Toulouse III, Toulouse, France

Published online: 23 September 2024

interactions and the growth of sea surface temperature (SST) anomalies under stochastic forcing. Besides the coastal oceanic wave activity of equatorial origin, eastward propagating extra-tropical atmospheric disturbances in the path of the subtropical jet streams (Rahn and Garreaud 2014) can also act as a noise forcing for local ocean–atmosphere instabilities to develop. As a result, persistent SST anomalies can grow independently of the basin-scale modes. Such SST anomalies have been observed in all EBUS and have been termed "Coastal Niño events" because of their dynamic similarities to their basin-scale counterparts. For instance, the Benguela Niño, consisting in an SST warming off the coast of Angola and Northern South Africa represents such type of events (Shannon et al. 1986; Lübbecke et al. 2010). More recently such coastal warmings have also been documented in other EBUS: Ningaloo Niño in Australia (Feng et al. 2013; Tozuka et al. 2014), Dakar Niño in Senegal (Oettli et al. 2016), California Niño in California (Simpson 1983), and Chile Niño in Chile (Xue et al. 2020). Off Peru, coastal Niño events also take place (Takahashi and Martinez 2019). The growth of these events can be broadly interpreted as resulting from a "coastal Bjerknes feedback" (Kataoka et al. 2014; Yuan and Yamagata 2014; Xue et al. 2020; Oettli et al. 2021) in which anomalous alongshore low level winds impact upwelling processes generating SST anomalies, that in turn can influence the zonal gradients of atmospheric pressure reinforcing the initial wind anomalies. However, since they take place in upwelling systems in which the cool SST favors a shallow Marine Boundary Layer (MBL), SST-low stratus cloud feedback (Clement et al. 2009) may be also important for these events to develop (Xue et al. 2020).

Here we focus on Chile Niño/Niña (CN) events that develop off Central Chile, a region under the direct influence of ENSO through both oceanic and atmospheric teleconnections (Cai et al. 2020; Sprintall et al. 2020). SST variability associated with CN accounts for up to 40% of the total variance of SST anomalies off the coast of north and central Chile (Fig. 1a) and can thus result in impacts in the marine and terrestrial ecosystems through producing stresses on fauna. For instance, Tongoy bay (30°S), a hotspot of the scallop aquaculture industry in Chile experiences episodes of warming and hypoxic conditions (Ramajo et al. 2019) that might be related to CN events. CN events are also associated with an increase in surface air temperature in the northern and central Chile continental region (Xue et al. 2021), favoring warmer than usual conditions in an already dry climate. The worst wildfires in the Chilean history of austral summer 2017 were preceded by a Chile Niño event (McWethy et al. 2018; Garreaud et al. 2019), and the burned area from wildfires in central Chile between 2004 and 2023 is correlated with CN SST anomalies (Cordero et al. 2024). In addition, CN events are associated with the development the South Pacific Meridional Mode (Xue et al. 2020; Dewitte et al. 2023) that also yields anomalous conditions at the scale of the South Eastern Pacific with potentially remote impacts. Considering the likely important societal implications of impacts due to CN, Xue et al. (2021) further investigated their predictability in the SINTEX-F2 coupled model (Luo et al. 2005). They showed that they can be predicted up to 3-month lead. However they note that the skill of the SINTEX-F2 system depends on whether or not events co-occur with ENSO. Events not preceded by ENSO are in particular less predictable. Therefore, accurate prediction of CN events remains a challenge.

A related concern is the degree to which climate prediction models are effective in accurately representing CN statistics and their changes in a warmer climate. This is relevant since CN can be considered as Marine Heat Waves (MHWs), i.e. episodes of anomalously warm surface waters in the ocean. Although MHWs are usually considered as warming events lasting a few days (Hobday et al. 2016), several studies define them using monthly mean data (Xu

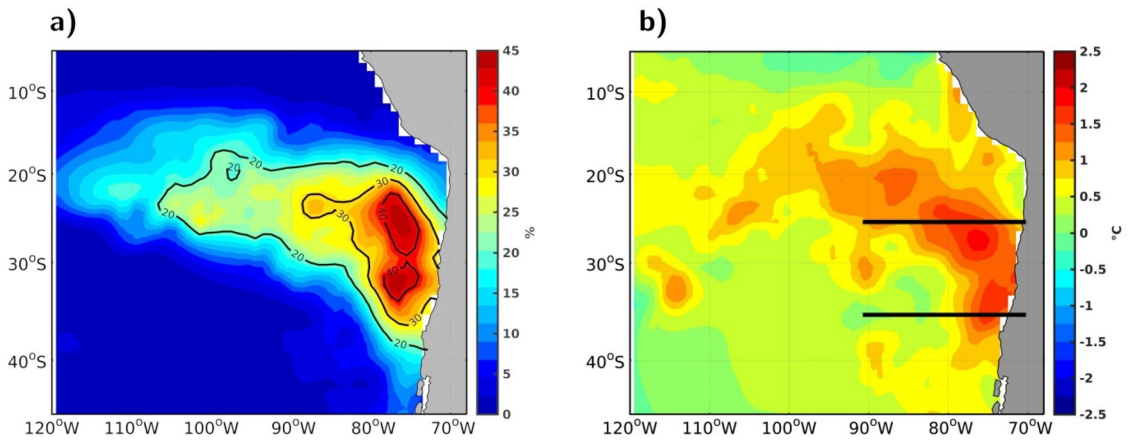

Fig. 1 **a** Explained variance of SST anomalies over 1948–2020 from observations, by CN. **b** Observed monthly SST anomalies in March 1980. Black lines show the zonal sections used in Fig. 3

et al. 2022; Amaya et al. 2023) and therefore coastal Niños that last several months could also be considered as MHWs. MHWs lasting a few days have drawn the interest of the scientific community in recent decades because they have increased in frequency and duration in most of the global ocean since the early twentieth century (Holbrook et al. 2020b; Oliver et al. 2018), and are also projected to continue increasing globally for the next decades under the influence of climate change (Frölicher et al. 2018; Oliver et al. 2019). Consequently, this raises the question of whether CN events will increase in frequency and amplitude in the future. It is noteworthy that the oceanic region along the coast of Peru and Chile (so-called Humboldt system) is projected to experience significant changes in its mean circulation and variability. Not only ENSO is projected to increase in variability (Cai et al. 2018, 2021) and persistence (Carréric et al. 2020; Lopez et al. 2022) in the future climate, but climate model projections also consistently indicate an increase in mid-latitudes upwelling favorable winds in the future associated with a strengthening and poleward shift of the mid-latitude low-pressure systems (Rykaczewski et al. 2015). Note that this is not necessarily the case for tropical EBUS (Oettli et al. 2021). Therefore whether or not CN will increase in frequency and/or intensity in the future climate remains an open question.

Here we tackle this issue taking advantage of the Coupled Model Intercomparison Project phases 5 (CMIP5) and 6 (CMIP6). As a first step, the skill of the CMIP models in simulating CN variability is evaluated. Despite the persistent warm bias along the coast of Chile in these models, we find that most models simulate realistically the CN pattern, which allows the investigation of their future evolution under anthropogenic forcing using the climate projection scenarios of CMIP5 and 6.

The paper is organized as follows: Sect. 2 describes the data and methods used. Section 3 provides an assessment of the CMIP models' skill in simulating the CN properties. Section 4 is an analysis of the changes in variability associated with CN events due to global warming and its relationship with that of remote drivers. Section 5 discusses the results and provides a conceptual view of competing processes at work to explain the CN property changes, along with concluding remarks.

2 Data and methods

2.1 Data sets

The observational monthly SST data used is retrieved from the Hadley Center data set (Rayner et al. 2003) which has a 1° resolution and covers the period 1948–2020. The monthly 10-m wind and sea level pressure data is taken from the National Centers for Environmental Prediction/National Center for Atmospheric Research (NCEP/NCAR) Reanalysis 1 (Kalnay et al. 1996) for the same time period. Monthly data of sea water potential temperature is obtained from the GLORYS12V1 product of the CMEMS reanalysis (Lellouche et al. 2021) with a horizontal resolution of 1/12° and 50 vertical levels for the period 1993–2020.

We analyze monthly outputs from 19 CMIP5 models and 43 CMIP6 models. The CMIP5 sub-group of 19 models was selected based on their ability to simulate realistically ENSO diversity (Cai et al. 2018) and to contrast with that of CMIP6 models in order to evaluate if our results are dependent on the generation of coupled models and to increase the ensemble size. We used historical runs (1920–2014) and simulations under greenhouse forcing from the RCP8.5 and SSP5-8.5 scenario (2015–2100). Models' names and their respective grid size are provided in Table 1. In most diagnostics, we treated the 62 models as a unique ensemble.

2.2 Methods

Prior to any analysis, all the model raw data is bilinearly interpolated onto a common global grid of $1° \times 1.25°$ (latitude x longitude). Also, all observed and model anomalies are linearly detrended prior to carrying out statistical analyses. The period used for the historical runs is 1920–2014 and for future projections 2015–2100.

We characterize ENSO variability in the tropics using the E and C indices of Takahashi et al. (2011) defined as $E = (PC1 — PC2)/\sqrt{2}$ and $C = (PC1 + PC2)/\sqrt{2}$, where PC1 and PC2 correspond to the first and second normalized principal components, respectively, of the first two EOF (Empirical Orthogonal Function) modes of SST monthly anomalies in the tropical Pacific (12°S-12°N, 120°E-70°W). E and C are orthogonal by construction, therefore their correlation at zero-lag is zero. Here, the E index accounts for El Niño events in the eastern Pacific and most of the extreme El Niño events, whereas the C index accounts for El Niño and La Niña events in the central Pacific. To characterize ENSO probability distribution, we also estimated its asymmetry based on the value of the first coefficient of the quadratic fit of PC2 onto PC1, i.e., $PC2(t) = \alpha \cdot [PC1(t)]^2 + \beta \cdot PC1(t) + \gamma$, which follows Karamperidou et al. (2017). This provides, in particular, a metric for models' ability to realistically simulate the Eastern Pacific El Niño pattern, which is considered a driver of CN events. The α values of the models are provided in Table 1.

A significant part of the subtropical SST variability off the coast of northern Chile is under the influence of ENSO through both atmospheric and oceanic teleconnections (Taschetto et al. 2020; Sprintall et al. 2020). Therefore, to define the Chile Niño/Niña index (CNI), we remove from the SST anomalies the ENSO influence through linear

Table 1 Description of the 62 CMIP5 and 6 models used

Archives	Name	Model center	ENSO non-linearity	Grid size (ocean/atmosphere)
CMIP5	BCC-CSM1-1-M	BCC/China	-0.21	360 x 232 / 320 x 160
	CCSM4	NCAR/United States	-0.53	320 x 384 / 288 x 192
	CESM1-BCG	NSF-DOE-NCAR/United states	-0.15	320 x 384 / 288 x 192
	CESM1-CAM5	NSF-DOE-NCAR/United states	-0.40	320 x 384 / 288 x 192
	CMCC-CM	CMCC/Italy	-0.17	182 x 149 / 480 x 240
	CMCC-CMS	CMCC/Italy	-0.31	182 x 149 / 192 x 96
	CMCC-CESM	CMCC/Italy	-0.22	182 x 149 / 96 x 48
	CNRM-CM5	CNRM-CERFACS/France	-0.26	362 x 292 / 256 x 128
	GFDL-CM3	NOAA-GFDL/United States	-0.30	144 x 90 / 240 x 121
	GFDL-ESM2G	NOAA-GFDL/United States	-0.03	360 x 210 / 144 x 90
	GFDL-ESM2M	NOAA-GFDL/United States	-0.49	360 x 200 / 144 x 90
	GISS-E2-H	NASA-GISS/United States	-0.27	144 x 90 / 240 x 121
	GISS-E2-R	NASA-GISS/United States	-0.26	144 x 90 / 144 x 90
	FGOALS-s2	LASG-IAP/China	-0.23	360 x 196/ 128 x 108
	FIO-ESM	FIO/China	-0.56	320 x 384 / 128 x 64
	IPSL-CM5B-LR	IPSL/France	-0.13	182 x 149/ 96 x 96
	MIROC5	MIROC/Japan	-0.43	256 x 128/ 240 x 121
	MPI-ESM-LR	MPI-M/Germany	-0.05	192 x 96 / 240 x 121
	MRI-CGCM3	MRI/Japan	-0.19	320 x 160 / 240 x 121
CMIP6	ACCESS-CM2	CSIRO-ARCCSS/Australia	-0.08	360 x 300 / 192 x 144
	ACCESS-ESM1-5	CSIRO/Australia	0.01	360 x 300 / 192 x 145
	AWI-CM-1-1-MR	AWI/Germany	0.03	(unstructured) /384 x 192
	BCC-CSM2-MR	BCC/China	-0.05	360 x 232 / 320 x 160
	CMCC-ESM2	CMCC/Italy	-0.51	362 x 292 / 288 x 192
	CNRM-CM6-1-HR	CNRM-CERFACS/France	-0.06	1442 x 1050 / 720 x 360
	CanESM5	CCCma/Canada	-0.03	360 x 291 / 128 x 64
	CanESM5-CanOE	CCCma/Canada	-0.02	360 x 291 / 128 x 64
	CAMS-CSM1-0	CAMS/China	-0.29	360 x 200 / 320 x 160
	CAS-ESM2-0	CAS/China	-0.23	360 x 196 / 256 x 128
	CMCC-CM2-SR5	CMCC/Italy	-0.16	362 x 292 / 288 x 192
	CNRM-CM6-1	CNRM-CERFACS/France	-0.16	362 x 294 / 256 x 128
	CNRM-ESM2-1	CNRM-CERFACS/France	-0.08	362 x 294 / 256 x 128
	EC-Earth3-CC	EC-Earth-Consortium	-0.26	362 x 292 / 512 x 256
	EC-Earth3	EC-Earth-Consortium	-0.13	362 x 292 / 512 x 256

Table 1 (continued)

	EC-Earth3-Veg	EC-Earth-Consortium	-0.13	362 x 292 / 512 x 256
	EC-Earth3-Veg-LR	EC-Earth-Consortium	-0.26	362 x 292 / 320 x 160
	FGOALS-f3-L	CAS/China	-0.43	360 x 218 / 288 x 180
	FGOALS-g3	CAS/China	-0.08	360 x 218 / 180 x 80
	GISS-E2-1-H	NASA-GISS/United States	-0.39	144 x 90 / 144 x 90
	GISS-E2-1-G	NASA-GISS/United States	-0.46	144 x 90 / 144 x 90
	GFDL-ESM4	NOAA-GFDL/United States	-0.16	720 x 576 / 288 x 190
	HadGEM3-GC31-LL	MOHC NERC/United Kingdom	-0.14	360 x 330 / 192 x 144
	HadGEM3-GC31-MM	MOHC/United Kingdom	-0.19	1440 x 1205 / 432 x 324
	INM-CM4-8	INM/Russia	-0.01	360 x 180 / 180 x 120
	INM-CM5-0	INM/Russia	0.04	360 x 180 / 180 x 120
	IPSL-CM6A-LR	IPSL/France	-0.06	362 x 332 / 144 x 143
	KACE-1-0-G	NIMS-KMA/Republic of Korea	-0.11	360 x 200 / 192 x 144
	KIOST-ESM	KIOST/Republic of Korea	-0.17	360 x 200 / 192 x 96
	MIROC6	MIROC/Japan	-0.33	360 x 256 / 256 x 128
	MIROC-ES2L	MIROC/Japan	-0.42	360 x 256 / 128 x 64
	MPI-ESM1-2-HR	MPI-M DWD DKRZ/Germany	-0.14	802 x 404 / 384 x 192
	MPI-ESM1-2-LR	MPI-M AWI DKRZ DWD/Germany	-0.15	256 x 220 / 192 x 96
	MRI-ESM2-0	MRI/Japan	-0.37	360 x 363 / 320 x 160
	MCM-UA-1-0	UA/United States	0.23	192 x 80 / 96 x 80
	NESM3	NUIST/China	-0.06	362 x 292 / 192 x 96
	UKESM1-0-LL	MOHC NERC NIMS-KMA NIWA/United Kingdom, Republic of Korea and New Zealand	-0.24	360 x 330 / 192 x 144
	CESM2	NCAR/United States	-0.30	320 x 384 / 288 x 192
	CESM2-WACCM	NCAR/United States	-0.24	320 x 384 / 288 x 192
	E3SM-1-1	E3SM-Project RUBISCO/United States	-0.03	360 x 180 / 360 x 180
	NorESM2-LM	NCC/Norway	-0.22	360 x 385 / 144 x 96
	NorESM2-MM	NCC/Norway	-0.17	360 x 385 / 288 x 192
	TaiESM1	AS-RCEC/Taiwan	-0.43	320 x 384 / 288 x 192
Observations	HadISST/NCEP-NCAR		-0.31	

Following Karamperidou et al. (2017) we quantify ENSO non-linearity using the value α of the first coefficient in the quadratic fit $PC2(t) = \alpha\,[PC1(t)]^2 + \beta\,PC1(t) + \gamma$, where PC1 and PC2 are the time series of the first two EOF modes of SST anomalies in the tropical Pacific. Models in blue correspond to the ones that are skillful in simulating the observed ENSO non-linearity and conform the group that is used to study the future variability of Chile Niño/Niña

regression. The CNI is then defined as the principal component of the first EOF mode of the residual SST anomalies over the region (80°W-70°W; 35°S-20°S). This follows Xue et al. (2020), except that here the influence of ENSO is removed using two ENSO indices instead of one, because at least two indices are required to properly describe ENSO diversity (Takahashi et al. 2011; Capotondi et al. 2015). This also eases the interpretation of the CNI variability since it is by construction independent of ENSO at zero lag. This is also required here for an objective comparison of the CMIP models since the ENSO pattern does not necessarily have the same projection onto the E and C modes amongst the models. The spatial pattern of CN is obtained by linearly regressing the normalized CNI onto the SST anomaly fields.

Since extra-tropical disturbances and their modulation by the South Pacific Anticyclone (Rahn and Garreaud 2014) can act as a noise forcing to CN, we also consider the South Pacific Oscillation (SPO) index as defined by You and Furtado (2017). An EOF analysis is performed onto the sea level pressure (SLP) anomaly fields in the region (10°S-45°S; 160°W–70°W) and the SPO index corresponds to the

normalized principal component of the first EOF mode of variability.

3 Characterization of Chile Niño/Niña in CMIP models

As a first step, we evaluate the models' skill in accounting for the main features of CN events. Figure 2a and d show the SST spatial pattern for observations and the model ensemble, respectively. It indicates that the models simulate realistically the CN pattern, with comparable magnitude and peak amplitude located in the same latitude range than the observations. Noteworthy the dispersion among the models (blue contours in Fig. 2d) does not peak in the region of maximum amplitude but to the west and in a narrow region along the coast. The mean explained variance of 65% ± 9% is however lower than the observed value of 80%, which reflects dispersion amongst models outside the core region of CN (rectangle in Fig. 2a), as will be seen later on. The spatial correlation (100°W-70°W, 45°S-10°S) between the simulated and the observed patterns is always larger than 0.65 (Figure S1 in Supplementary Information). The agreement between models and observations is also good in terms of the relationship between winds and CN SST anomalies at zero lag: The maximum wind anomaly magnitude value in the core region of the CN reaches 0.33 m s^{-1} for both observations and models, and their respective mean values in the CN region are 0.14 m s^{-1} and 0.22 m s^{-1}. Discrepancy between models and observations are more pronounced in terms of the seasonality of the CNI. Figure 2b and e display the climatological variance of the CNI for observations and the model ensemble. Despite an overall comparable magnitude and seasonality (i.e. peak variance around austral summer), the maximum variance takes place in April in the models, two months after the observed peak in February. Looking at the models individually, we notice that 37 out of 62 (60%) have their peak between February and April (Figure S2) while the rest have it in other months of the year. Additionally, we examined the asymmetry of the CNI as a function of calendar months (Fig. 2c and f). The skewness value for a specific calendar month represents the skewness of the three consecutive months centered around that calendar

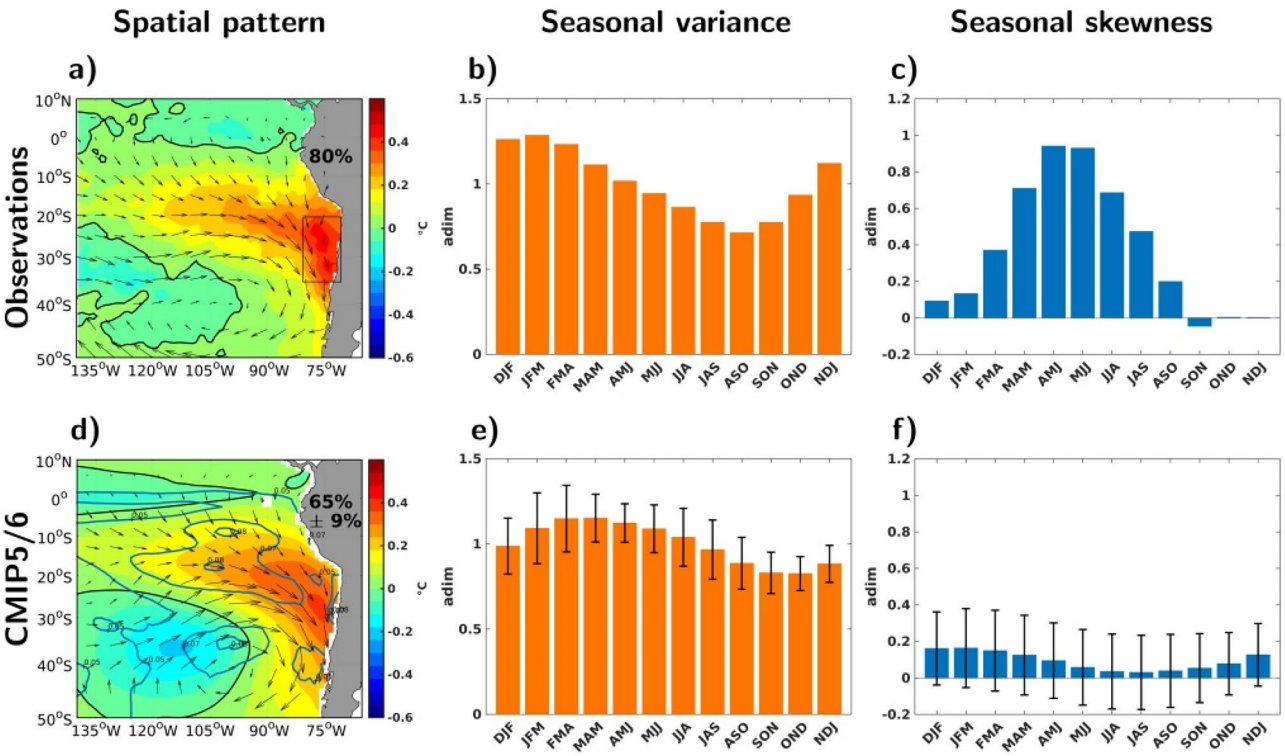

Fig. 2 CN characteristics in observations and CMIP models: **a**, **d** Spatial pattern of CN obtained through a linear regression of the normalized CNI index onto SST anomalies (shading) and low-level wind anomalies (arrows) for **a** observations (Feb-1948 to May-2020) and **d** the ensemble mean of the 62 CMIP5/6 models. Explained variability of the first EOF mode is indicated in the map. Blue contours in **d** represent standard deviation of the SST patterns among the ensemble. **b**, **e** Seasonal variance of the CNI. **c**, **f** Seasonal skewness of the CNI. In **e** and **f** dispersion is shown as vertical segments on the bars. The size of the segment represents plus or minus the standard deviation amongst the ensemble

month. To quantify the asymmetry we use the normalized skewness (s), defined as:

$$s = \frac{\frac{1}{N}\sum_{i=1}^{N}\left(x_i - \bar{x}\right)^3}{\sigma^3}$$

where x_i is the i^{th} data point, N is the number of data (3 times the number of years, since we take 3 consecutive months per year for a given calendar month), $\bar{x}$ is the mean and σ is the standard deviation. The observed CN has a positive skewness most of the year, which we verified was due to the larger occurrence of Chile Niños than Chile Niñas rather than their difference in amplitude. Peak skewness is reached in austral winter (Fig. 2c). In contrast, the model ensemble fails to reproduce this feature, presenting a weak positive skewness on average most of the year (Fig. 2f). Noteworthy, most CN events in observations occur in austral summer when the skewness is rather low. In order to understand why the CNI skewness is weak in the models, we further analyzed the number of events in observations and in the models. CN events are defined based on the value of the CNI: when the CNI is above 1σ (below – 1σ) a Chile Niño (Niña) event takes place. The event ends when the CNI values no longer satisfy this condition for at least two consecutive months. We found that there are 4.4 Chile Niño and 3.9 Chile Niña events per decade in the observational record, while for the models there is an average of 4.6 Chile Niño and 4.7 Chile Niña events per decade (See Figure S3). Hence the frequency of occurrence of warm events is similar between observations and models, but the models tend to simulate more (+ 18%) cold events.

To document the time evolution of CN events, we carry out a composite evolution analysis in two zonal sections, at 25°S and 35°S (Fig. 1b) for both warm and cold events (Fig. 3). The peak of amplitude of Chile Niño is comparable to the one in observations, being located also at the same distance from the coast in the 25°S section and attached to the coast at the 35°S section. In the case of the Chile Niña events the peak location is similar to observations, but the models tend to simulate a slightly weaker anomaly. Despite the overall good agreement, a notable discrepancy between the observations and the models is the larger persistence of SST anomalies in the observations compared to the model composite. Warm events last ~ 2 months more in the observations than in the models. This is more pronounced for Chile Niña events, for which the persistence (~ 8 months) is more than twice the build-up time (~ 3 months) in the observations, while the models feature a comparable span of the developing and decaying phases (i.e. ~ 2 months). This lack of temporal asymmetry between the developing and decaying phases in the models can also explain the weaker skewness of the CNI compared the observations (Fig. 2c, f), e.g., a longer persistence of strong Chile Niño events may positively skew the distribution.

Xue et al. (2020) showed that the CN growth rate involves a coastal Bjerknes feedback in which shortwave radiation and mixing also play a key role. This indicates that the vertical structure of temperature variability is a key parameter in CN dynamics. We thus inspect the mean vertical structure of temperature of the CN events in the models (Fig. 4). The CMEMS reanalysis (1993–2020) is used as a benchmark for comparison. The latter has a CN pattern that closely resembles the one from HadISST (Figure S4). Similarly to the methodology used to obtain the surface pattern, here we calculated the linear regression of the CNI in a zonal section at 25°S for the reanalysis data and the model ensemble. The comparison indicates a relatively good agreement between models and reanalysis data in terms of the spatial pattern and amplitude, considering that models have significant mean state bias in the coastal region (Dewitte et al. 2023). The peak warming during CN is confined to the first 50 m consistent with the dominant role of heat flux forcing on SST anomalies (Xue et al. 2020). Although the reanalysis data shows a negative anomaly of temperature near the coast (between 50 and 100 m), this is not statistically significant to the 95% level. On the other hand, models display a high dispersion of coastal warming between 10 and 100 m depth (Fig. 4c). This could indicate coastal processes involved in the development of CN events that are not well resolved in some of the models, such as the passing of coastal trapped Kelvin waves (Pizarro et al. 2001). To summarize, the results indicate that the CMIP models have some skill in simulating the main characteristics of CN events, which motivates us to document how they simulate their changes in properties in the future.

4 Chile Niño/Niña under global warming

4.1 Changes in variance and frequency

Since the definition of CN is tied to ENSO variability, hereafter we select a sub-group of models that realistically simulate ENSO characteristics. In particular, we are interested in models that can simulate the different type of events; consisting, in general, in strong eastern Pacific events and moderate amplitude events that peak in the central equatorial Pacific (Takahashi et al. 2011). This is referred to as ENSO diversity in the ENSO literature (Capotondi et al. 2015). A compact measure of the ENSO diversity has been proposed by Karamperidou et al. (2017), which consists in the value α of the first coefficient in the quadratic fit of PC1 and PC2 time series of the first two EOF modes of SST anomalies in the tropical Pacific (see Methods). Here we thus select a group of 36 models that have a value of α that reaches at

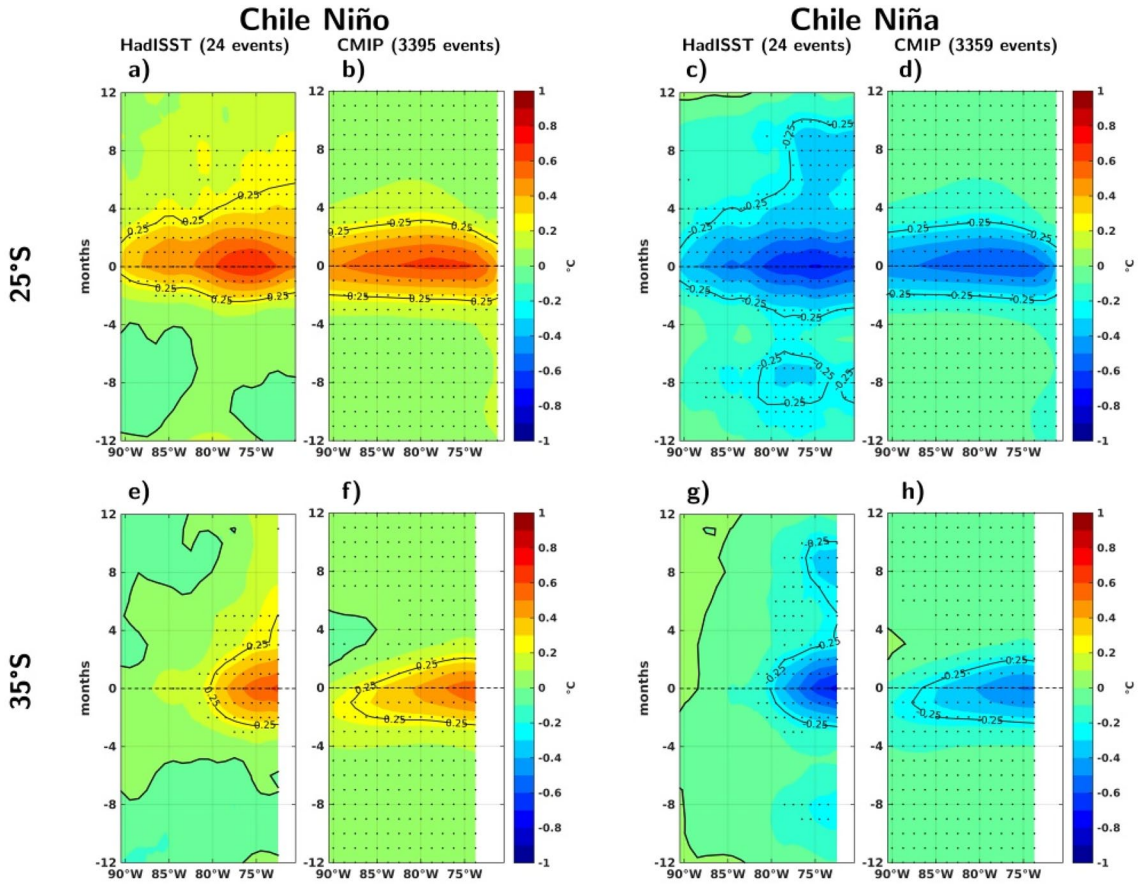

Fig. 3 Composite evolution of SST anomalies for Chile Niño (**a**, **b**, **e**, **f**) and Chile Niña (**c**, **d**, **g**, **h**) events in zonal sections at 25°S (top) and 35°S (bottom) for observations (**a**, **c**, **e**, **g**) and multimodel ensemble (**b**, **d**, **f**, **h**). Hovmöller diagrams show positive (negative) values on the y-axis that indicate months after (before) the peak of events. Dots indicate values that are significant to the 95% level based on a t-test. Number of events is indicated in parentheses

least 50% of the observed value of − 0.31 (models in blue font in Table 1).

To study the projected changes in CN we assess the change in variability of the CNI index. Since the latter is normalized, the CNI of the RCP8.5/SSP5-8.5 scenario for each model is scaled by the projection of the spatial pattern onto that of the historical run. This procedure follows Carréric et al. (2020). Figure 5 displays the change in variability of the scaled CNI (in %) between the future and present climates. The results indicate that on average there is an increase in variability of the CNI of 3.2% (last red bar in Fig. 5). Although relatively small, the lower limit of dispersion does not reach zero and hence this increase is statistically significant based on a bootstrap test (see details in caption text of Fig. 5). Moreover, 24 out of 36 models (66.7%) show an increase in the variability of the CNI under the anthropogenic forcing scenario with a total mean increase in variability reaching 8% (±2.8%, obtained with the bootstrap method). Most of the models show a variation inferior to 12% with the exception of the CESM2-WACCM model, which reaches a value of nearly 40%. Removing this outlier from the ensemble mean yields an increase in CNI variance of 2.2%, which is still statistically significant. When calculating the change of CNI variance between the present and future climates for each month of the year it is found that the increase is very similar throughout the year, therefore this change is not seasonally dependent (not shown). Noteworthy, this increase in variance is associated with the increase of the amplitude of the CN events rather than the increase in the number of events. In fact, the frequency of occurrence of CN does not change between the present and future climates (not shown).

Considering the relatively low increase in variance reflecting a rather weak consensus amongst the models, we separate the ensemble into two groups in order to interpret the dispersion in the change in variance of the CNI. The two groups consist in the models for which the CNI variance increase (IVG) or decrease (DVG). Figure 6 displays the mean difference between the future and present SST patterns for the 36 models and for these two groups.

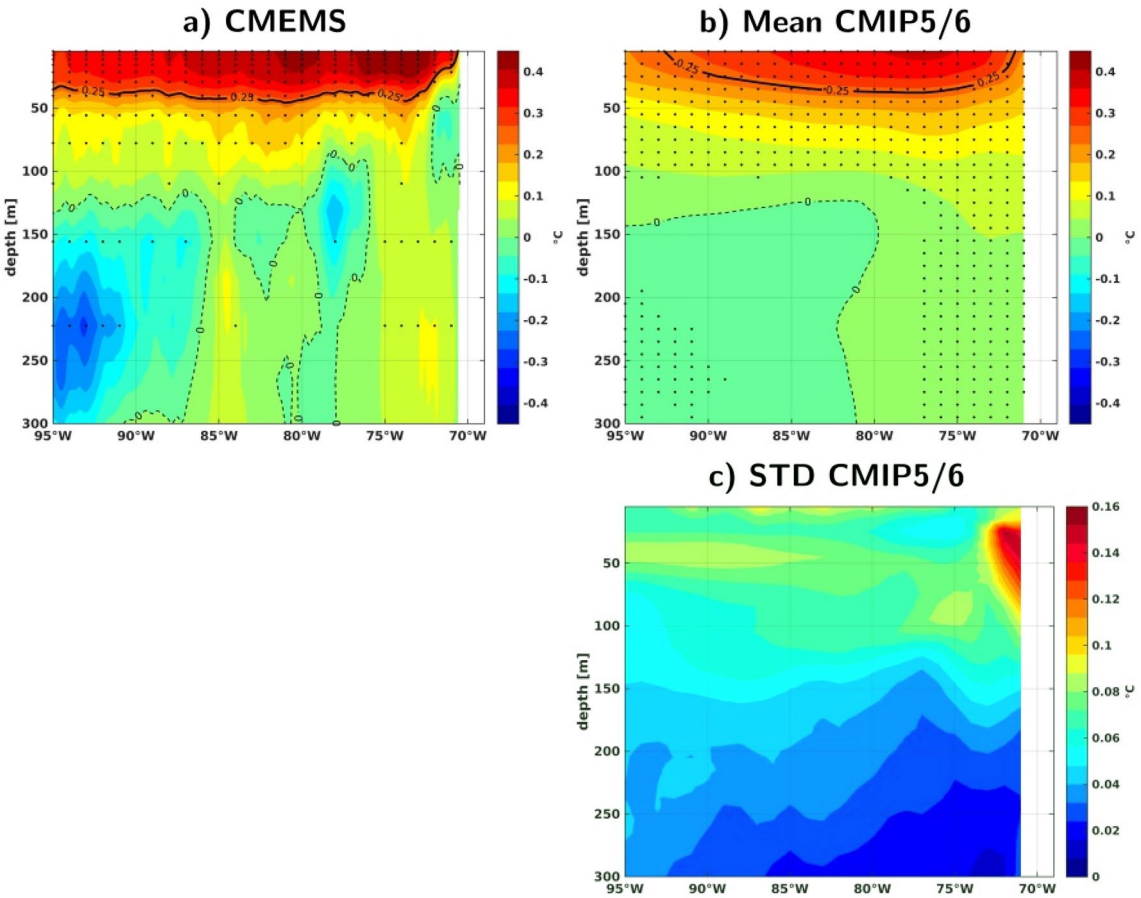

Fig. 4 CN pattern in depth, at 25°S, obtained by linearly regressing CNI onto sea water potential temperature anomalies. **a** CMEMS reanalysis (1993–2020), **b** ensemble mean of 55 CMIP5 and 6 models. **c** Dispersion (standard deviation) amongst the models. Black stippling in **a** indicates values that are significant to the 95% level based on a t-test, and stippling in **b** indicates points where at least 75% of the models agree on the sign

The IVG pattern shows a statistically significant increase in amplitude (+ 0.05 °C) near the coast, between 25°S and 35°S, a region where also at least 75% of the models agree on the sign of pattern change. On the other hand, the DVG group shows a statistically significant decrease in amplitude in the off-shore oceanic region between 15°S and 25°S, with no statistically significant change in the core region of CN. The peak changes are approximately co-located with the maximum amplitude of the mean historical pattern (black contours in Fig. 6), with the IVG group exhibiting a more coastal mean pattern than the DVG group. This suggests different mechanisms at work in the development of the CN events for the two groups. This will be discussed later in Sect. 5.

4.2 Changes in the drivers of Chile Niño/Niña

In order to elucidate what drives the variability changes in CN and interpret the above results, we first analyze the relationship between the CNI and the E index. Although the CNI and the E index are independent at zero lag by construction, an El Niño event can yield warm SST anomalies ~ 6 months off central Chile after the El Niño peak. This coastal SST warming has been shown to be associated with the development of the South Pacific Meridional Mode (SPMM) in some models (Dewitte et al. 2023). Here we observe that CN tends to be associated with the development of SPMM events (Figure S5), which motivates to investigate the CN-ENSO relationship. The lagged-correlation between the CNI and the E index as a function of calendar month is presented in Fig. 7 for both the model ensemble and the observations. It indicates that the E index tends to be ahead the CNI by ~ 10 months in austral spring (winter) in the model ensemble (the observations), although such relationship

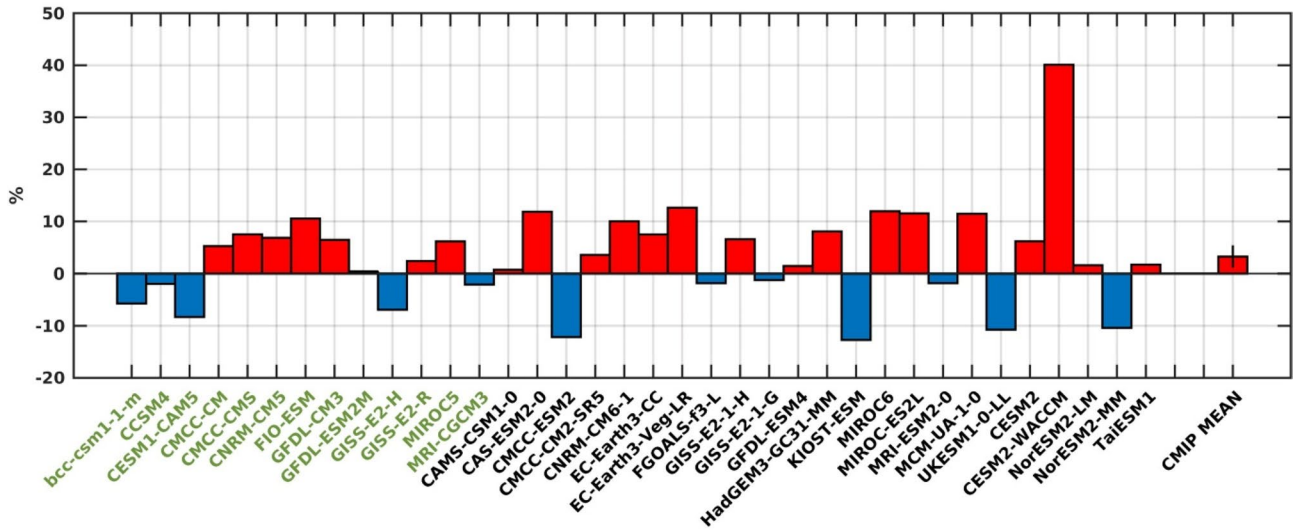

Fig. 5 Change in variability of the CNI between the present (1920–2014) and future (2015–2100) climate for the 36 selected models. Green (black) font in the x-axis corresponds to CMIP5 (CMIP6) models. The last bar shows the multi-model mean with its corresponding confidence interval as a vertical segment. The confidence interval is obtained using a bootstrap test consisting in randomly re-sampling 10,000 times the changes in variance amongst the models. 36 models are considered on each re-sampling with repetition allowed. Standard deviation is calculated for each realization and then the standard deviation among these 10,000 values is calculated. This value is used to plot the upper and lower limits of dispersion

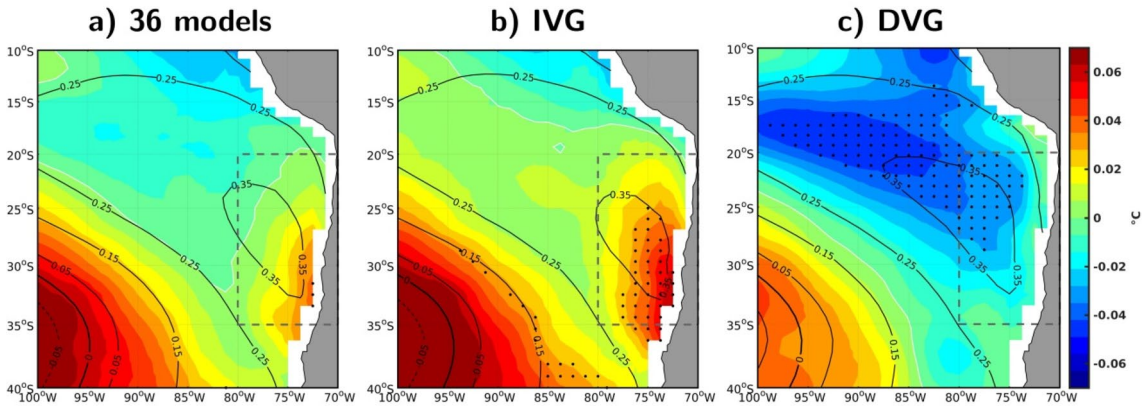

Fig. 6 Projected change in CN SST pattern (in °C). Shading corresponds to the projected pattern (SSP585/RCP8.5) minus the historical pattern for **a** the subset of 36 models, **b** IVG (24 models) and **c** DVG (12 models). Black contours show the mean CN pattern for the historical runs of each group. Black dots indicate where values are significant to the 90% level based on a t-test and where at least 75% of the models agree on the sign of change. Dashed rectangles indicate CN region

results from no more than ~ 29% of the CN being preceded by an ENSO event, which is diversely simulated by the models (Fig. 8). Note that the model ensemble fails in simulating the positive relationship between CNI and the E index for positive lag (CNI ahead of E) evidenced in the observations.

We now focus on a mid-latitude driver of the CN, the South Pacific Oscillation (SPO) that consists in a meridional dipole of sea level pressure (SLP) anomalies extending from 60°S to 35°S (You and Furtado 2017). Its northern node represents the variability of the South Pacific subtropical high intensity and the southeasterly trade winds associated to it. Xue et al. (2020) identifies the SPO as a precursor signal of CN. They have shown that a negative (positive) anomaly of SLP forms 2–3 months ahead a Chile Niño (Niña) event, suggesting that the weakened (strengthened) coastal winds trigger this event. To examine the SPO-CN relationship, the lagged-correlation between the CNI and the SPO index is estimated as function of calendar month (Fig. 9). The results indicate that the model ensemble simulates realistically such a lagged relationship as well as its seasonality. In particular,

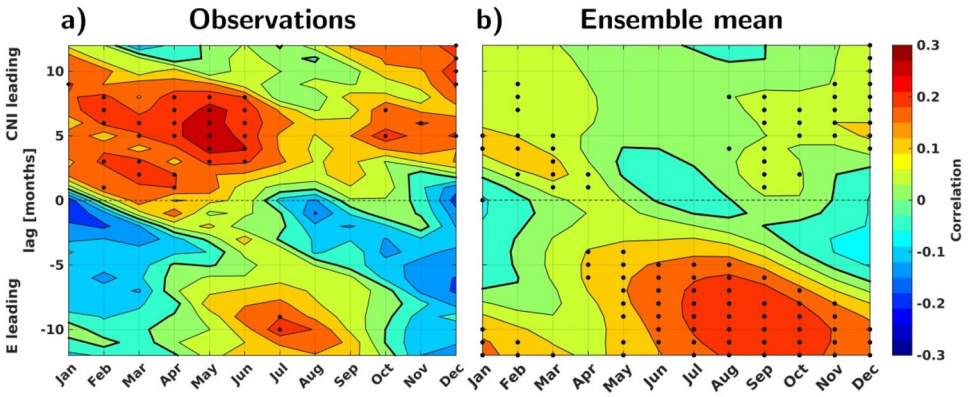

Fig. 7 Lagged correlation between CNI and E index as a function of calendar month for **a** observations and **b** ensemble mean of the 36 selected models. Months in the x-axis correspond to CNI months. Dots indicate values that are significant to the 95% level based on a t-test. For **b** black dots also indicate where at least 75% of the models agree on the correlation sign

the peak correlation (c ~ 0.5) between the SPO index and the CNI is reached between March and May with the SPO index preceding CNI by ~ 2 months. The correlation pattern is slightly slanted towards larger phase difference from May to September. An estimated 29% CN events are preceded by an SPO event (ahead by 0 to 4 months) in the observations, while in the model ensemble this percentage varies between 35 to 55%, which weakly changes with the mean climate conditions (Figure S6).

ENSO and SPO can be thus considered as drivers of the CN events in the models. It is worth noticing that although by construction the E index and CNI are uncorrelated at zero lag, they exhibit a strong linear relationship at ~ 10 months lag (E ahead of CNI). It is now useful to document ENSO changes in variability from the present and future climates, as well as the SPO changes, in order to interpret the results of Fig. 5. Cai et al. (2018, 2020) showed that the E index increases in variance in the future, which we verified here from our model ensemble. In particular there is a significant increase of 9.2% of the E variance in the 36 selected models here (Fig. 10a) with 70% of the models exhibiting an increase. This does not translate into a comparable increase in the CNI variance because only about one fourth of the CN events are preceded by an El Niño event. However, it may explain why there are more models that showcase an increase in CNI variance than a decrease. From the 24 models that showcase an increase in CNI variance (red bars in Fig. 5), 17 (71%) evidence an increase in the variance of the E index (red diamonds in Fig. 10a). Additionally, from these 17 models 10 evidence an increase in the frequency of Chile Niño events that are preceded by Eastern Pacific El Niño events (black line in Figure S7), of which 9 also showcase an increase in the occurrence of Eastern Pacific El Niño events (red line in Figure S7). Also, 5 models showcase a decrease in event frequency in both CNI and the E index (Figure S7). While there is no clear linear relationship between changes in variance of the CNI and E indices (c = 0.07), these considerations suggest that the change in CNI variance is linked to the change in the statistics of ENSO. If ENSO is favorable for the development of CN and that the increase in ENSO variance in the future does not translate in a proportional increase in the CNI variance, we may hypothesize that this is due to changes in the other driver of CN, the SPO. Figure 10b displays the changes in variance of the SPO index

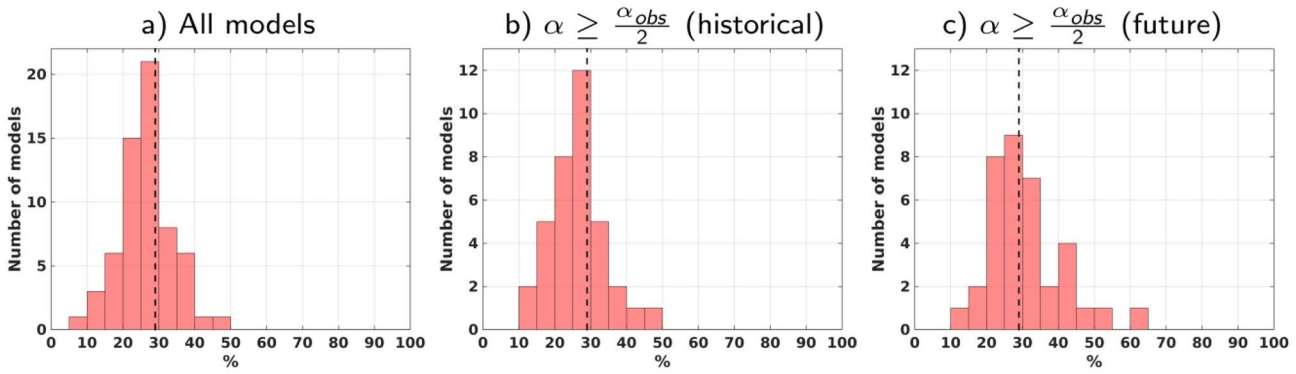

Fig. 8 Percentage of CN events preceded by eastern Pacific ENSO events: Histogram for the number of models by percentage for **a** All models, **b** historical runs of the 36 selected models and **c** projected scenarios (RCP8.5/SSP5-8.5) of the 36 selected models. The black dashed vertical line indicates the value for the observations

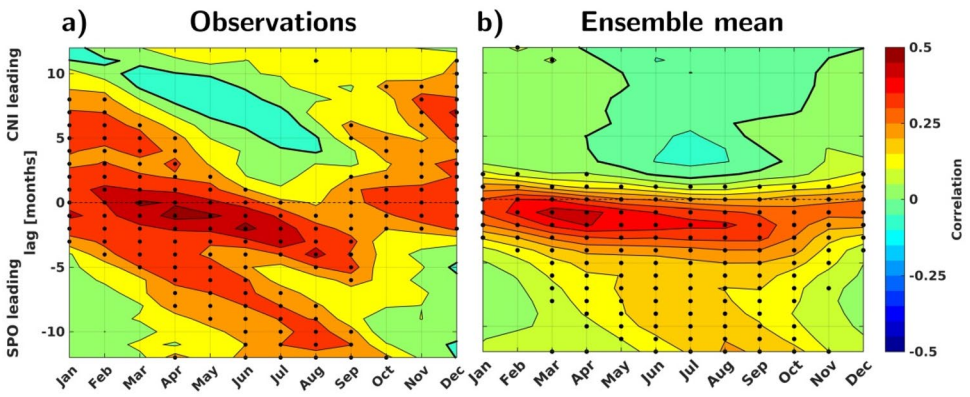

Fig. 9 Lagged correlation between CNI and SPO index as a function of calendar month for **a** observations and **b** ensemble mean of the 36 selected models. Months in the x-axis correspond to CNI months. Dots indicate values that are significant to the 95% level based on a t-test. For **b** black dots also indicate where at least 75% of the models agree on the correlation sign

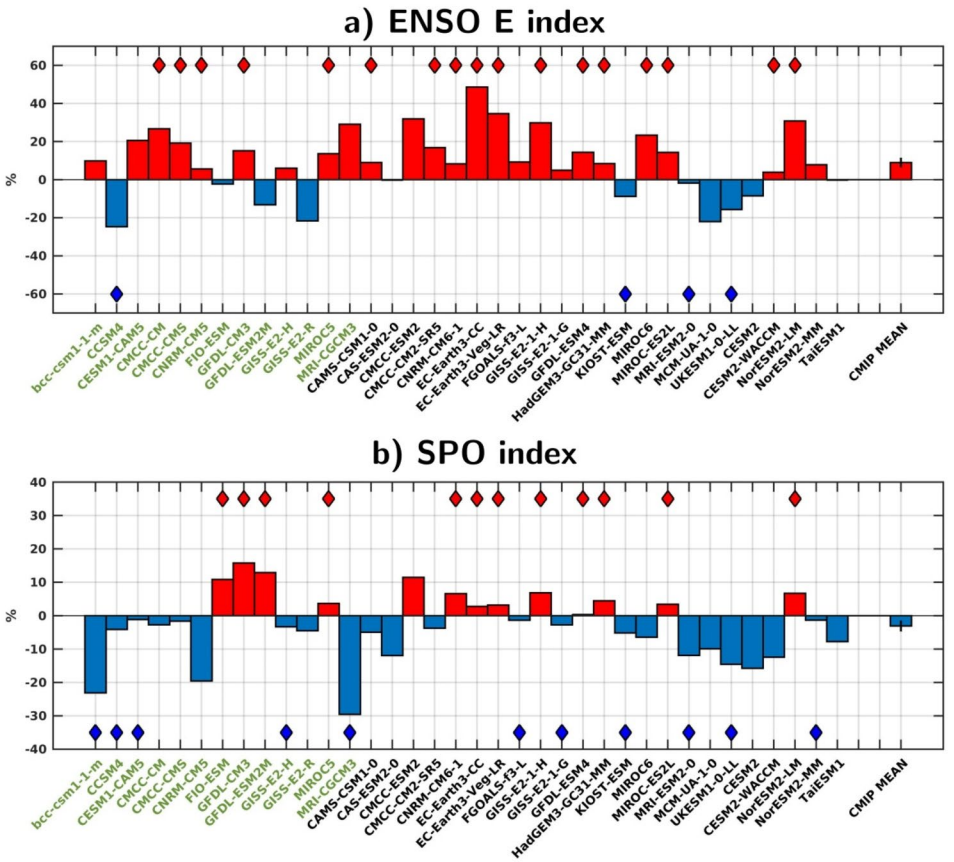

Fig. 10 Change in variability of the **a** E index and **b** SPO index between the present (1920–2014) and future (2015–2100) climate for the 36 selected models. Green (black) font in the x-axis corresponds to CMIP5 (CMIP6) models. Multi-model mean is shown with its corresponding confidence interval as a vertical segment. The confidence interval is obtained using a bootstrap method following the methodology of Cai et al, (2018), as in Fig. 5. Red (blue) diamonds indicate models for which the sign of change in CNI and E/SPO is positive (negative) for both indices

between the present and future climates. It indicates that there is a tendency towards a reduction in the variance of the SPO although the consensus among models is low, with 23 (64%) experiencing a decrease in variability. There is no linear relationship between the changes in variance of the CNI index and that of the SPO index amongst the models (c = 0.03), for instance, the CMCC-ESM2 model evidences a large increase in variance for both the SPO and E indices, but has a strong reduction in the CNI variance. Therefore, although we observe a relationship between changes in E and CNI variability this is not linear and this aspect cannot be explained by changes in the SPO.

Summarizing, amongst the two climate drivers of CN events, only ENSO evidences changes in the future that could explain the increase in CNI variance. However, the increase in CNI variance is not correlated to either that of the E index (c = 0.08) nor that of the SPO index (c = 0.03) amongst the models, which suggests that the change in CNI variability is not only controlled by changes in external forcing but also by alterations in local processes due to changes in the mean conditions. In the following, we document

changes in the mean conditions controlling key processes of the mixed-layer and marine boundary layer (MBL) budgets during CN.

4.3 Changes in local processes

As a starting point, we rely on first principles and focus on few key local processes known to take place and be altered by global warming in the region of interest. Three features of the mean circulation are considered: oceanic stratification, MBL stability and surface winds. So-called feedbacks are evaluated, which is based on simple linear regressions between relevant variables. This approach is commonly used to address processes in a multi-model framework (e.g. Planton et al. (2021) for ENSO).

4.3.1 Thermocline feedback

Along the coast of Chile, changes in oceanic stratification (measured as the difference between mean temperature at 5 m and 75 m) are manifested as a significant deepening of the mean thermocline rather than a clear shoaling of the mixed-layer (Figure S8). The former yields a reduction (increase) of the thermocline feedback along the coast (in the open ocean) off Central Chile as diagnosed by the change in the regression coefficient between the CNI and thermocline depth anomalies (Fig. 11a). The results indicate a zonal dipole pattern of the changes within the CN region, which can be interpreted as resulting from a flattening of the isotherms due to the stronger coastal warming with regards to the off-shore region. This dipole pattern is also evidenced in other quantities, as will be seen, and we thus chose to consider two regions within the CN region accounting for this dipole pattern (see rectangles in Fig. 11). There is thus a reduction of the thermocline feedback in the coastal box, while it increases in the off-shore box (see Table 2). The reduction in the coastal box implies a less effective equatorial oceanic teleconnection through coastal Kelvin wave-induced vertical advection, while the increase in the off-shore box may favor the forcing of SST anomalies by ENSO-induced extra-tropical Rossby waves radiating from the coast or locally forced by the wind (Vega et al. 2003).

4.3.2 Mixing feedback

This feedback represents the control of the rate of change in temperature by the climatological surface heat flux under changing mixed layer heat capacity ($\frac{\partial T}{dt} = -\frac{\overline{Q}}{\rho c_p \overline{h}^2} h'$, see Eq. 2 in Xue et al. (2020)). It is estimated as the regression coefficient between mixed-layer depth anomalies and CNI. Xue et al (2020) refers to it as the heat capacity anomaly effect and suggest it is a key process during the development of CN events. We call it here "mixing feedback" because, through

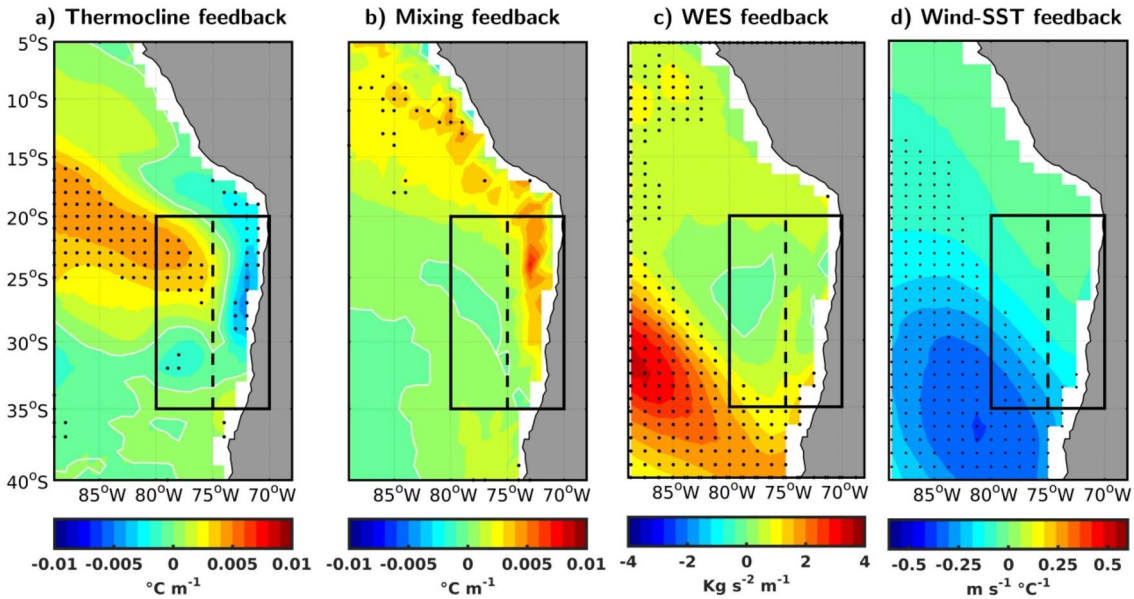

Fig. 11 Mean changes of local physical processes in the ensemble of models between future projections and historical runs (future minus historical). **a** Linear regression coefficient between the CNI and thermocline depth anomalies, **b** linear regression coefficient between the CNI and mixed layer depth anomalies, **c** WESp value and **d** linear regression coefficient between meridional low-level wind anomalies and CNI. The regression coefficients of **d** have been multiplied by – 1. Black dots indicate values that are significant to the 95% level based on a t-test. The black box divided by a segmented line shows the offshore and coastal CN regions used to calculate the averaged values on Table 2

Table 2 Mean values of local physical processes inside the coastal (75°W-70°W, 35°S-20°S and offshore (80°W–75°W, 35°S–20°S) boxes of the CN region

	WES feedback		**Mixing feedback**		**Thermocline feedback**		**Wind-SST feedback**		**MBL stability**	
	WESp (V) [W s m^{-2}]		β ($CNI(t) \approx \beta \cdot H_{mix}(t)$) [°C m^{-1}]		α ($CNI(t) \approx \alpha \cdot H(t)$) [°C m^{-1}]		-η ($V_{wind}(t) \approx \eta \cdot CNI(t)$) [m s^{-1} ° C^{-1}]		LTS [°C]	
	Off-shore	Coast	Off-shore	Coast	Off-shore	Coast	Off-shore	Coast	Off-shore	Coast
Present (1920–2014)	10.64	8.31	-6.6×10^{-3}	-3.2×10^{-3}	6×10^{-3}	9.9×10^{-3}	0.85	0.44	-13.02	-12.11
Future (2015–2100)	11.11	8.88	-6.1×10^{-3}	-0.6×10^{-3}	7.4×10^{-3}	8.3×10^{-3}	0.68	0.36	-12.05	-12.01
Future – Present (Bold when significant)	0.47 (4.4%)	0.57 (6.9%)	0.6×10^{-3} (8.34%)	**2.6×10^{-3} (80.74%)**	**1.4×10^{-3} (23.54%)**	**-1.6×10^{-3} (−16.1%)**	**−0.16 (−19.24%)**	**−0.08 (−18.12%)**	**0.97 (7.45%)**	0.1 (0.84%)
Correlation among models with change in CNI variance	0.16	0.21	−0.3	0.29	0.69	0.5	0.35	0.25	-0.01	0.06

Boxes are shown in Fig. 11. The definition of each feedback is provided in the main text of Sect. 4.3. The statistical significance is obtained using a bootstrap method where the values for the models are randomly re-sampled 10.000 times, taking only N models on each re-sampling (N is the closer integer to 80% of the total number of available models) and allowing repetition. This is done for historical and future projections. Standard deviation is calculated for each realization and then the standard deviation among these 10.000 values is calculated. If the interval defined by this standard deviation and the mean value does not overlap between present and future then the difference is considered statistically significant

the regression, it may also encapsulate other processes that are sensitive to the changes in the mixed-layer depth (e.g. vertical diffusivity, vertical entrainment). The results indicate that it is mostly a damping process (i.e. negative regression coefficient) and that it is significantly altered in the future climate in the coastal region with a reduction amounting to 80% (Table 2 and Fig. 11b). Its reduction implies that warm CN events are less damped by this process in the future climate in the coastal domain, which is favorable for the growth of CN.

4.3.3 Wind-evaporation-SST (WES) feedback

The WES feedback refers to the mutual reinforcement between winds and SST through evaporative processes and has been shown to be a key mechanism in mid-latitude systems (Xie and Philander 1994; Chang et al. 1997). Its strength is tightly linked to the background surface winds. Off-central Chile, the equatorward winds increase in the future climate (Figure S9), which results from the poleward expansion of the Hadley cell (Lu et al. 2007; Goubanova et al. 2011; Rykaczewski et al. 2015). The increase in meridional winds implies an increase in the WES feedback (Wang 2010). This was confirmed through assessing the sensitivity of latent heat flux to meridional winds, or Wind-Evaporation-SST parameter (WESp) defined as:

$$WESp = \frac{-LH \cdot V}{W^2}$$

where LH is the latent heat, V is the meridional wind, W is the wind speed ($W = \sqrt{u^2 + v^2 + \hat{w}^2}$) and $\hat{w}$ is a background wind speed used to account for higher frequency variance with a value of $\hat{w}$=4 m s^{-1} (Czaja et al. 2002; Vimont 2010; Martinez-Villalobos and Vimont 2016; Sanchez et al. 2019). WESp is expressed in units of Kg s^{-2} m^{-1}. As expected, we find that the WESp increases significantly where the increase in low-level meridional wind is the largest and significant (Figure S9), that is in the region of the Coastal Jet and to the west of the CN region (Fig. 11c). This implies a larger sensitivity of SST to latent heat changes at regional scale in the future climate, which is favorable to the increase in variance of CNI.

4.3.4 Wind-SST feedback

Another compact measure of how strongly the atmospheric winds respond to SST anomalies is the wind-SST feedback (Guilyardi 2006) that encapsulates the collective role of the processes discussed above. In coastal upwelling regions it is a damping process due to the dominance of Ekman dynamics (i.e. inverse relationship between along-shore winds and SST anomalies). It is here inferred from the regression coefficient between the CNI and the meridional low-level winds anomalies. For the sake of clarity, the regression coefficient

is multiplied by – 1, so that an enhanced coupling strength implies that it makes it easier for a small SST or wind perturbations to grow and develop as a CN event, and the contrary otherwise. The results, displayed in Fig. 11d and Table 2, indicate that the coupling strength weakens on average off central Chile, with a peak and significant change to the South of the CN core region where the low-level atmospheric coastal jet extends from further south (Garreaud and Muñoz 2005). Over this region (40°S–25°S, 85°W–75°W), 32 out of the 36 models present a mean weaker coupling (not shown) with no clear separation between the IVG and DVG in terms of mean value of the changes. Therefore, the change in coupling strength between the present and future climates in the model ensemble is favorable for the damping of CN variability in the future climate.

Taken together, the results suggest that although changes in the WES and mixing feedbacks will favor the development of events near the coast, coastal Kelvin waves of tropical origin will be a less efficient trigger for them. On the other hand, changes in the WES and thermocline feedbacks will make the offshore region more susceptible to the development of events through atmospheric forcing and Rossby waves. However this will be counterbalanced by a reduction in the Wind-SST feedback. As a summary, we provide the Table 3 that synthesizes the changes in feedbacks and their relationship with the changes in the mean circulation.

5 Discussion and concluding remarks

We evaluated how the historical runs of 62 CMIP5/6 models represent the main characteristics of CN. Despite the relatively coarse resolution of the models with regards to their ability to simulate coastal processes, they are found to be skillful in simulating the SST spatial pattern of CN events. Most of the models (62%) also realistically simulate the seasonal evolution of the CNI although 18 models show a shift in the peak of variability up to 2 seasons. The main deficiency of the models regards their tendency to simulate too many Chile Niña events than observed resulting in a weak positive skewness of the CNI compared to observations. This relatively good performance of the CMIP models in simulating CN characteristics contrast with their limited skill for coastal El Niño events off Peru (Chen and Jin 2023; Martinez-Villalobos et al. 2024).

The good performance of the CMIP models in simulating the CN provided an incentive for investigating its future changes in a sub-group of models (36) that realistically simulate ENSO variability. We find that 24 (12) out of 36 models project an increase (decrease) in the variability of CNI under climate change, resulting in an average 3.2% increase in variance. This increase in variance is associated with the increase in amplitude of the CN events (Fig. 6) rather than the increase in the frequency of the events (not shown). The increase in amplitude/variance of CN events is interpreted as resulting from both changes in external forcing and local processes: (1) Increased ENSO variance is propitious for the enhancement of SST off central Chile during CN events linked to ENSO (one fourth of the events). We also find that equatorial zonal wind anomalies not necessarily linked to ENSO in the western-central equatorial Pacific are enhanced between the present and future climates (not shown), which favors the excitation of CN events by coastal disturbances originating from the equatorial region (e.g. coastal Kelvin waves). On the other hand, the SPO variance is reduced, which reduces one of the sources of noise forcing to CN events through the fluctuations of the mid-latitude pressure systems. The reduced variance (also evidenced in the daily and monthly meridional winds in the CN region (not shown)) can be interpreted as resulting from the increase in MBL stability. In a warming world, there is a tendency for a greater atmospheric warming in subtropical regions above the boundary layer than at the surface (Miller 1997). Warm-above-cool anomalies imply enhanced low-tropospheric stability (LTS) that can reduce the vertical motion and impede convection. The LTS can be measured by the difference between the 700 hPa potential temperature and SST and is usually strong in the southeast Pacific stratus region (> 18 °C; Klein and Hartmann 1993). Consistently, we find that stability is enhanced in the CN region (See Table 2 and Figure S10). (2) Regarding local processes, there are also competing effects due to changes in the mean conditions. Amongst the four local feedbacks diagnosed here (see Sect. 4.2, Table 2), two experience changes favorable to the damping of CN growth: the thermocline feedback along the coast and the wind-SST feedback. The reduced wind-SST

Table 3 Changes in the strength of feedbacks between the present and future climates and related changes in mean circulation

Local process	Projected changes in strength	Related changes in mean circulation
Thermocline feedback	Increase (decrease) in the oceanic (coastal) region	Deepening of thermocline and on-shoreward flattening of isotherms
Mixing feedback	Decrease	Increase in vertical stratification
WES feedback	Increase	Intensification of meridional wind speed
Wind-SST feedback	Decrease	Deepening thermocline and increase in MBL stability

feedback can be interpreted as resulting from the reduction in the thermocline feedback and the increase in MBL stability. It is worth to mention that the mean changes in the SST-low cloud feedback (Xue et al 2020) were also quantified in 31 models for which cloud cover data was available. Low cloud cover was defined as the values at 680 hPa or higher (average between 680 and 1000 hPa), based on the International Satellite Cloud Climatology Project (ISCCP) definition (Rossow and Schiffer 1999). The results indicate a slight mean increase of this feedback but that is not significant due to the large dispersion amongst the models (not shown).

The reduced thermocline feedback along the coast weakens the equatorial oceanic teleconnection to the central Chile region since wave activity originating from the equatorial region is less effective in inducing mean vertical advection of anomalous temperature. Amongst all the feedbacks, only the change in thermocline feedback correlates significantly to the change in CNI variance ($c = 0{,}69$ and $c = 0.50$ for the off-shore and coastal boxes, respectively, see Table 2), suggesting the importance of thermal vertical changes in constraining the CN amplitude increase. Interestingly we find that vertical stratification is slightly increased between the present and future climates (Figure S8c) but the changes are not significant. On the other hand, the mean thermocline experiences a significant deepening that is larger along the coast than in the open ocean (Figure S8b). The latter is consistent with the weakening of the thermocline feedback along the coast because it becomes more difficult for thermocline fluctuations to influence SST. Consistently, we also find that the changes in mean thermocline depth are correlated to changes in CNI variance amongst models ($c = 0.4$ for the CN region). This however does not mean that the other feedbacks are not influential but their changes may be more diversely simulated amongst the models with also compensating effects between them. In particular the mean warm SST bias along the coast of Chile in the CMIP models (Dewitte et al. 2023) varies significantly amongst them. Since mean state constrains the balance between feedbacks locally, we may expect a different sensitivity of this balance to mean state changes. This issue would deserve further research, which could be based on the experimentation with a coupled model (e.g. Goubanova et al. (2019)), as well as an explicit quantification of the mixed-layer heat budget. Overall, our study contrasts with previous works suggesting that MHWs will increase in intensity and frequency in the future climate (Frölicher et al. 2018; Oliver et al. 2019). For CN, we only find a mild increase in intensity with no increase in frequency, which results from compensating effects in terms of both external remote forcing (i.e. ENSO versus SPO) and local feedbacks. Nonetheless, while no strong changes in CN variability are observed, the increase in mean SST in the future climate will make that the threshold with respect to the baseline climate for a CN to take place will be reached more often in the future, which still poses challenges to marine ecosystems and coastal communities. In that respect our results may be useful to create a narrative for the local stakeholders that emphasizes the critical role of long-term changes in mean SST rather that of extremes, which can provide guidance for adaptation strategies. Our results also questions if coastal Niño events in other EBUS (e.g., Benguela Niño, and Ningaloo Niño) will undergo comparable changes considering that the other tropical basins are also projected to experience robust changes in variability in a warmer climate (Atlantic: Crespo et al. 2022; Indian ocean: Sun et al. 2022). Inter-hemispheric asymmetry in the response of these coastal events to climate change may be also expected due to differences in equatorial oceanic teleconnections between the two hemispheres and the asymmetry in the climate change SST patterns in the mid-latitude EBUS (Rykaczewski et al. 2015; Watt-Meyer et al. 2019).

Supplementary Information The online version contains supplementary material available at https://doi.org/10.1007/s00382-024-07434-5.

Acknowledgements We thank Pr. S.-I. An and Dr. Laurent Terray for stimulating discussions. EC acknowledges support from the Agencia Nacional de Investigación y Desarrollo (ANID)/Programa Formación de Capital Humano Avanzado (PFCHA) (Doctorado Becas Chile/2019-72200310). BD acknowledges support from ANID (Concurso de Fortalecimiento al Desarrollo Científico de Centros Regionales 2020-R20F0008-CEAZA, Anillo Eclipse ACT210071, and Centro de Investigación Oceanográfica en el Pacífico Sur-Oriental COPAS COASTAL FB210021, Fondecyt Regular N°1231174). BD also acknowledges support from the French National program LEFE (Les Enveloppes Fluides et l'Environnement) through the SEPICAF project, the EU H2020 FutureMares project (Theme LC-CLA-06-2019, Grant agreement No 869300) and the CE2COAST project funded by ANR through the 2019 "Joint Transnational Call on Next Generation Climate Science in Europe for Oceans" initiated by JPI Climate and JPI Oceans. CM acknowledges support from Proyecto ANID Fondecyt Postdoctorado código 3200621, Data Observatory Foundation ANID Technology Center No. DO210001 and Fondecyt Regular N°1231174. This work was granted access to the HPC resources of CALMIP supercomputing center under the allocation 2023-1044.

Funding Open access funding provided by Université Toulouse III - Paul Sabatier. EC acknowledges support from the Agencia Nacional de Investigación y Desarrollo (ANID)/Programa Formación de Capital Humano Avanzado (PFCHA) (Doctorado Becas Chile/2019–72200310). BD acknowledges support from ANID (Concurso de Fortalecimiento al Desarrollo Científico de Centros Regionales 2020-R20F0008-CEAZA, Anillo Eclipse ACT210071, and Centro de Investigación Oceanográfica en el Pacífico Sur-Oriental COPAS COASTAL FB210021, Fondecyt Regular N°1231174). BD also acknowledges support from the French National program LEFE (Les Enveloppes Fluides et l'Environnement) through the SEPICAF project. CM acknowledges support from Proyecto ANID Fondecyt Postdoctorado código 3200621, Data Observatory Foundation ANID Technology Center No. DO210001 and Fondecyt Regular N°1231174. This work was granted access to the HPC resources of CALMIP supercomputing center under the allocation 2023–1044.

Data availability The monthly SST data from HadISST used here is available at https://www.metoffice.gov.uk/hadobs/hadisst/data/download.html. The monthly 10-m winds and sea level pressure fields from

NCEP/NCAR Reanalysis 1 are available at https://psl.noaa.gov/data/gridded/data.ncep.reanalysis.html. The monthly data of sea water potential temperature from the GLORYS12V1 product of the CMEMS reanalysis can be downloaded from https://data.marine.copernicus.eu/product/GLOBAL_MULTIYEAR_PHY_001_030/services. CMIP5 and 6 data is available through several portals that can be found at https://pcmdi.llnl.gov/mips/cmip5/data-access-getting-started.html and https://pcmdi.llnl.gov/CMIP6/, respectively.

Declarations

Conflict of interests The authors have no relevant financial or non-financial interests to disclose.

References

Amaya DJ, Jacox MG, Alexander MA, Scott JD, Deser C, Capotondi A, Phillips AS (2023) Bottom marine heatwaves along the continental shelves of North America. Nat Commun 14(1):1038

Cai W, Wang G, Dewitte B, Wu L, Santoso A, Takahashi K et al (2018) Increased variability of eastern Pacific El Niño under greenhouse warming. Nature 564:201–206. https://doi.org/10.1038/s41586-018-0776-9

Cai W, McPhaden MJ, Grimm AM, Rodrigues RR, Taschetto AS, Garreaud RD et al (2020) Climate impacts of the El Niño– southern oscillation on South America. Nat Rev Earth Environ 1:215–231. https://doi.org/10.1038/s43017-020-0040-3

Cai W, Santoso A, Collins M, Dewitte B, Karamperidou C, Kug JS, Zhong W (2021) Changing El Niño-Southern oscillation in a warming climate. Nat Rev Earth Environ 2(9):628–644

Capotondi, A., Wittenberg, A. T., Newman, M., Di Lorenzo, E., Yu, J. Y., Braconnot, P., ... & Yeh, S. W. (2015). Understanding ENSO diversity. *Bulletin of the American Meteorological Society*, *96*(6), 921–938.

Carréric A, Dewitte B, Cai W, Capotondi A, Takahashi K, Yeh SW, Guémas V (2020) Change in strong Eastern Pacific El Niño events dynamics in the warming climate. Clim Dyn 54:901–918

Chang P, Ji L, Li H (1997) A decadal climate variation in the tropical Atlantic Ocean from thermodynamic air–sea interactions. Nature 385:516–518. https://doi.org/10.1038/385516a0

Chen HC, Jin FF (2023) The mechanism of boreal summer SSTA phase-locking in the far eastern Pacific. NPJ Clim Atmos Sci 6(1):138

Clement AC, Burgman R, Norris JR (2009) Observational and model evidence for positive low-level cloud feedback. Science 325(5939):460–464. https://doi.org/10.1126/science.1171255

Cordero RR, Feron S, Damiani A, Carrasco J, Karas C, Wang C, Beaulieu A (2024) Extreme fire weather in Chile driven by climate change and El Niño-Southern Oscillation (ENSO). Sci Rep 14(1):1974

Crespo LR, Prigent A, Keenlyside N, Koseki S, Svendsen L, Richter I, Sánchez-Gómez E (2022) Weakening of the Atlantic Niño variability under global warming. Nat Clim Chang 12:822–827. https://doi.org/10.1038/s41558-022-01453-y

Czaja A, Van der Vaart P, Marshall J (2002) A diagnostic study of the role of remote forcing in tropical Atlantic variability. J Clim 15(22):3280–3290

Dewitte B, Concha E, Saavedra D, Pizarro O, Martinez-Villalobos C, Gushchina D, Ramos M, Montecinos A (2023) The ENSO-induced South Pacific Meridional Mode. Front Clim 4:1080978. https://doi.org/10.3389/fclim.2022.1080978

Feng M, McPhaden MJ, Xie SP, Hafner JL (2013) Niña forces unprecedented Leeuwin Current warming in 2011. Sci Rep 3:1277. https://doi.org/10.1038/srep01277

Frölicher TL, Fischer EM, Gruber N (2018) Marine heatwaves under global warming. Nature 560:360–364. https://doi.org/10.1038/s41586-018-0383-9

Garreaud RD, Muñoz RC (2005) The low-level jet off the west coast of subtropical South America: structure and variability. Mon Wea Rev 133:2246–2260

Garreaud RD, Boisier JP, Rondanelli R, Montecinos A, Sepúlveda HH, Veloso-Aguila D (2019) The central Chile mega drought (2010–2018): a climate dynamics perspective. Int J Climatol 40(1):421–439

Goubanova K, Echevin V, Dewitte B, Codron F, Takahashi K, Terray P, Vrac M (2011) Statistical downscaling of sea-surface wind over the Peru-Chile upwelling region: diagnosing the impact of climate change from the IPSL-CM4 model. Clim Dyn 36:1365–1378

Goubanova K, Sanchez-Gomez E, Frauen C, Voldoire A (2019) Respective roles of remote and local wind stress forcings in the development of warm SST errors in the South-Eastern Tropical Atlantic in a coupled high-resolution model. Clim Dyn 52:1359–1382

Guilyardi E (2006) El Niño–mean state–seasonal cycle interactions in a multi-model ensemble. Clim Dyn 26:329–348

Hobday AJ, Alexander LV, Perkins SE, Smale DA, Straub SC, Oliver EC, Wernberg T (2016) A hierarchical approach to defining marine heatwaves. Progress Oceanogr 141:227–238

Holbrook NJ, Claar DC, Hobday AJ, McInnes KL, Oliver EC, Gupta AS, Zhang X (2020a) ENSO-driven ocean extremes and their ecosystem impacts. El Niño southern oscillation in a changing climate, 409–428

Holbrook NJ, Gupta AS, Oliver EC, Hobday AJ, Benthuysen JA, Scannell HA et al (2020b) Keeping pace with marine heatwaves. Nat Rev Earth Environ 1(9):482–493. https://doi.org/10.1038/s43017-020-0068-4

Kalnay E, Kanamitsu M, Kistler R, Collins W, Deaven D, Gandin L, Joseph D (1996) The NCEP/NCAR 40-year reanalysis project. Bull Am Meteorol Soc 77:437–472. https://doi.org/10.1175/1520-0477(1996)077%3c0437:TNYRP%3e2.0.CO;2

Karamperidou C, Jin FF, Conroy JL (2017) The importance of ENSO nonlinearities in tropical pacific response to external forcing. Clim Dyn 49:2695–2704

Kataoka T, Tozuka T, Behera S, Yamagata T (2014) On the Ningaloo Niño/niña Clim Dyn 43:1463–1482

Klein SA, Hartmann DL (1993) The seasonal cycle of low stratiform clouds. J Clim 6(8):1587–1606

Lellouche J-M, Greiner E, Bourdallé-Badie R et al (2021) The Copernicus global 1/12° oceanic and sea ice GLORYS12 reanalysis. Front Earth Sci 9:698876. https://doi.org/10.3389/feart.2021.698876

Lopez H, Lee SK, Kim D, Wittenberg AT, Yeh SW (2022) Projections of faster onset and slower decay of El Niño in the 21st century. Nat Commun 13(1):1915

Luo J-J, Masson S, Behera S, Shingu S, Yamagata T (2005) Seasonal climate predictability in a coupled OAGCM using a different approach for ensemble forecasts. J Clim 18(21):4474–4497. https://doi.org/10.1175/JCLI3526.1

Lu J, Vecchi GA, Reichler T (2007) Expansion of the Hadley cell under global warming. Geophys Res Lett 34:L06805. https://doi.org/10.1029/2006GL028443

Lübbecke JF, Böning CW, Keenlyside NS, Xie SP (2010) On the connection between Benguela and equatorial Atlantic Niños and the role of the South Atlantic anticyclone. J Geophys Res 115:C09015. https://doi.org/10.1029/2009JC005964

Martinez-Villalobos C, Vimont DJ (2016) The role of the mean state in meridional mode structure and growth. J Clim 29(10):3907–3921

Martinez-Villalobos C, Dewitte B, Garreaud RD, Loyola L (2024) Extreme coastal El Niño events are tightly linked to the development of the Pacific Meridional Modes. NPJ Clim Atmos Sci 7(1):123

McPhaden MJ, Zebiak SE, Glantz MH (2006) ENSO as an integrating concept in earth science. Science 314(5806):1740–1745

McWethy DB, Pauchard A, García RA, Holz A, González ME, Veblen TT, Currey B (2018) Landscape drivers of recent fire activity (2001–2017) in south-central Chile. PLoS ONE 13(8):e0201195

Miller RL (1997) Tropical thermostats and low cloud cover. J Clim 10(3):409–440

Oettli P, Morioka Y, Yamagata T (2016) A regional climate mode discovered in the North Atlantic: Dakar Niño/Niña. Sci Rep 6(1):18782. https://doi.org/10.1038/srep18782

Oettli P, Yuan C, Richter I (2021) The other coastal Niño/Niña—the Benguela, California, and Dakar Niños/Niñas. In *Tropical and Extratropical Air-Sea Interactions* (pp. 237–266). Elsevier.

Oliver ECJ, Markus GD, Michael TB, Pippa JM, Dan AS, Lisa VA, Jessica AB et al (2018) Longer and more frequent marine heatwaves over the past century. Nat Commun. https://doi.org/10.1038/s41467-018-03732-9

Oliver EC, Burrows MT, Donat MG, Sen Gupta A, Alexander LV, Perkins-Kirkpatrick SE, Smale DA (2019) Projected marine heatwaves in the 21st century and the potential for ecological impact. Front Mar Sci 6:734

Pizarro O, Clarke AJ, Van Gorder S (2001) El Niño sea level and currents along the South American coast: comparison of observations with theory. J Phys Oceanogr 31(7):1891–1903. https://doi.org/10.1175/1520-0485(2001)031%3c1891:ENOSLA%3e2.0.CO;2

Planton YY, Guilyardi E, Wittenberg AT, Lee J, Gleckler PJ, Bayr T, Voldoire A (2021) Evaluating climate models with the CLIVAR 2020 ENSO metrics package. Bull Am Meteorol Soc 102(2):E193–E217

Rahn DA, Garreaud RD (2014) A synoptic climatology of the near-surface wind along the west coast of South America. Int J Climatol 34(3):780–792

Ramajo L, Fernández C, Núñez Y, Caballero P, Lardies MA, Poupin MJ (2019) Physiological responses of juvenile Chilean scallops (*Argopecten purpuratus*) to isolated and combined environmental drivers of coastal upwelling. ICES J Mar Sci 76(6):1836–1849

Rayner NA, Parker DE, Horton EB, Folland CK, Alexander LV, Rowell DP et al (2003) Global analyses of sea surface temperature, sea ice, night marine air temperature since the late nineteenth century. J Geophys Res 108:2670. https://doi.org/10.1029/2002JD002670

Rossow WB, Schiffer RA (1999) Advances in understanding clouds from ISCCP. Bull Am Meteor Soc 80(11):2261–2288

Rykaczewski RR, Dunne JP, Sydeman WJ, García-Reyes M, Black BA, Bograd SJ (2015) Poleward displacement of coastal upwelling-favorable winds in the ocean's eastern boundary currents through the 21st century. Geophys Res Lett 42:6424–6431. https://doi.org/10.1002/2015GL064694

Sanchez SC, Amaya DJ, Miller AJ, Xie SP, Charles CD (2019) The Pacific Meridional Mode over the last millennium. Clim Dyn 53:3547–3560

Shannon LV, Boyd AJ, Brundrit GB, Taunton-Clark J (1986) On the existence of an El Niño-type phenomenon in the Benguela system. J Mar Res 44(3):495–520. https://doi.org/10.1357/002224086788403105

Simpson JJ (1983) Large-scale thermal anomalies in the California Current during the 1982–1983 El Niño. Geophys Res Lett 10(10):937–940

Sprintall, J., Cravatte, S., Dewitte, B., Du, Y., & Gupta, A. S. (2020). ENSO oceanic teleconnections. *El Niño southern oscillation in a changing climate*, 337–359.

Sun S, Fang Y, Zu Y, Liu L, Li K (2022) Increased occurrences of early Indian Ocean Dipole under global warming. Sci Adv 8(47):eadd6025

Takahashi K, Montecinos A, Goubanova K, Dewitte B (2011) ENSO regimes: Reinterpreting the canonical and Modoki El Niño. Geophys Res Lett 38:L10704. https://doi.org/10.1029/2011GL047364

Takahashi K, Martínez AG (2019) The very strong coastal El Niño in 1925 in the far-eastern Pacific. Clim Dyn 52(12):7389–7415

Taschetto AS, Ummenhofer CC, Stuecker MF, Dommenget D, Ashok K, Rodrigues RR, Yeh SW (2020) ENSO atmospheric teleconnections. El Niño southern oscillation in a changing climate, 309–335

Tozuka T, Kataoka T, Yamagata T (2014) Locally and remotely forced atmospheric circulation anomalies of Ningaloo Niño/Niña. Clim Dyn 43(7–8):2197–2205. https://doi.org/10.1007/s00382-013-2044-x

Vega A, du-Penhoat Y, Dewitte B, Pizarro O (2003) Equatorial forcing of interannual Rossby waves in the eastern South Pacific. Geophys Res Lett 30(5)

Vimont DJ (2010) Transient growth of thermodynamically coupled variations in the tropics under an equatorially symmetric mean state. J Clim 23(21):5771–5789

Wang F (2010) Thermodynamic coupled modes in the tropical atmosphere–ocean: an analytical solution. J Atmos Sci 67(5):1667–1677

Watt-Meyer O, Frierson DM, Fu Q (2019) Hemispheric asymmetry of tropical expansion under CO2 forcing. Geophys Res Lett 46(15):9231–9240

Xie S-P, Philander SGH (1994) A coupled ocean–atmosphere model of relevance to the ITCZ in the eastern Pacific. Tellus 46A:340–350. https://doi.org/10.1034/j.1600-0870.1994.t01-1-00001.x

Xu T, Newman M, Capotondi A, Stevenson S, Di Lorenzo E, Alexander MA (2022) An increase in marine heatwaves without significant changes in surface ocean temperature variability. Nat Commun 13(1):7396

Xue J, Luo J-J, Yuan C, Yamagata T (2020) Discovery of Chile Niño/Niña. Geophys Res Lett 47:e2019GL086468. https://doi.org/10.1029/2019GL086468

Xue J, Doi T, Luo JJ, Yuan C, Yamagata T (2021) Predictability of the Chile Niño/Niña. Geophys Res Lett 48(21):e2021GL095309.

You Y, Furtado JC (2017) The role of South Pacific atmospheric variability in the development of different types of ENSO. Geophys Res Lett 44:7438–7446. https://doi.org/10.1002/2017GL073475

Yuan C, Yamagata T (2014) California Niño/niña Scientific Reports 4(1):4801. https://doi.org/10.1038/srep04801